small structures
www.small-structures.com

In Search of Structure' Links Across Length Scales: Crossover Among Structural Motifs, Energetics, and Magic Systems in Subnanometer Transition Metals Clusters

Ernesto Garcia-Alfonso, Thantip Roongcharoen, Piotr Zuchowski, and Alessandro Fortunelli**

Clusters of transition metal (TM) elements are becoming increasingly important in our daily lives for a wide ensemble of applications in catalysis and bio-fields, for health, energy and environmental problems. To help build structure/property relationships for these critical materials, it is presented here, first, a systematic study and descriptor-based classification of the structure, energetics, and quantum properties of TM tetramers and hexamers via first-principles simulations. Then, the obtained database is analyzed to single out trends in energetic and structural quantities, and their connections with the corresponding quantities of macroscopic bulk and larger clusters. It is found that the correlations between the micro and the macro scale do exist, providing recognizable evolution patterns in terms of both size and atomic number. At the same time, exceptions to the observed trends (outliers), are encountered including "magic" or on the opposite fluxional clusters, and an effort to rationalize their occurrence in terms of electronic structure considerations is made.

1. Introduction

Subnanometer metal clusters represent a very active field of current research in materials science.[1] Their unique properties due to confinement phenomena at the extreme provide these systems (among other appealing properties) with a distinct chemistry, so that they have been increasingly used as effective and selective catalysts, especially when deposited on proper (e.g., metal-oxide or carbonaceous) supports.[2–8] Determining the clusters' most stable configurations represents the first step in building structure/property relationships. However, atomistic structures at this length scale are nontrivial and usually very different from known phases of the bulk or of larger aggregates, while structure determination of subnanometer systems present such difficulties to offer itself as a significant challenge in the field.[9,10] In this context, theoretical and computational studies can play a very important role if they are predictive enough to provide accurate results. Despite these challenges, research is producing a growing amount of information that can orient research and offer a general framework for interpreting and designing these materials. One of the intriguing observations suggests that trends exist in the periodic table of the elements, trends correlating structures at very different length scales, or in other words that chemical elements in the periodic table can be assigned common, intrinsic structural motifs evolving with size from the subnanoscale to the bulk. For example, a previous study showed that the structures of the lowest-energy configurations of 55-atom clusters (experimentally determined in agreement with computational predictions) do correlate with the bulk structures of the same elements for a wide set of transition metals (TM),[11] therefore linking nanometer and mesoscopic forms of matter. An inspection of the results of previous systematic theoretical studies[12] suggests that this holds true for even smaller (subnanometer) metal clusters. However, these indications have been followed only sporadically in the literature, despite the fact that spotting general trends would provide a deeper understanding and orient the search of systems with tailored performances.[13]

In the present work, we pursue this line of research and start filling the current lack of knowledge. We conduct a systematic computational investigation at the first-principles density-functional theory (DFT) level of the low-energy structures of 4-atom (tetramer) and 6-atom (hexamer) clusters in the gas phase, covering all the TM. We derive both the global minima and the first isomers, as well as selected energy barriers connecting the global minima with the first isomers. As we will see, tetramers and hexamers exhibit sufficient structural diversity to stand as significant examples, apart from their intrinsic interest in catalytic applications.[14,15] Even-number sizes such

E. Garcia-Alfonso, T. Roongcharoen, A. Fortunelli
CNR-ICCOM, Institute of Chemistry of OrganoMetallic Compounds
Consiglio Nazionale delle Ricerche
Via Giuseppe Moruzzi 1, 56124 Pisa, Italy
E-mail: ernestogarciaalfonso96@gmail.com; alessandro.fortunelli@cnr.it

P. Zuchowski
Institute of Physics
Nicolaus Copernicus University
Grudziądzka 5/7, 87-100 Toruń, Poland

The ORCID identification number(s) for the author(s) of this article can be found under https://doi.org/10.1002/sstr.202500345.

DOI: 10.1002/sstr.202500345

as tetramers and hexamers possess a closed *s*-shell that allows us to separate spin phenomena due to the incomplete *d*-shell electrons. Moreover, with this choice we integrate recent work on odd-atom subnanometer clusters, such as trimers[16–18] and pentamers[19–21] (see also interesting conical intersection phenomena[22]). Our aim is to build structure/energy relationships for these systems, where energy is connected with properties, that is, response functions, via its various derivatives.[23] We therefore analyze the obtained results to spot trends in key geometric and energetic quantities, such as: structural motifs of the global minimum, energy gap and selected energy barriers between global minima and lowest-lying isomers, global quantities such as electronegativity and hardness. We are so able to: 1) find and demonstrate links (correlations) between structural motifs at the subnanoscale with those typical of larger, even macroscopic length scales, 2) illustrate the crossover among the different structural motifs as a function of atomic number, 3) single out "magic" cluster with exceptional structural stability and separate them from fluxional[24,25] clusters, and 4) correlate structural and electronic properties. All the results of this study are publicly shared on an open repository[26] to provide a database that can be used by other researchers for validation and further analysis.

The article is structured as follows. Section 2 introduces the theoretical approach and framework of our study. Morphology and energetics at the nanoscale, including classification and rationale are discussed in Section 3. Conclusions are presented in Section 4.

2. Theoretical Approach

We conducted DFT calculations using the Quantum Espresso package[27] with the PBEsol exchange and correlation functional (the Perdew–Burke–Ernzerhof functional[28] for solids)[29,30] and ultrasoft pseudopotentials (USPP).[31,32] In addition, a Grimme's D3 dispersion term was added to ensure the long-range dispersion interactions.[33] It is useful to note that the third row TM (Hf-Hg) have their f-electrons included in a large core, thus not explicitly described in the USPP we employ here. All calculations were performed spin-unrestricted, although some of the clusters are non magnetic. Electronic energy levels were broadened using a Gaussian smearing, σ, of 0.0005 Rydberg. Geometry relaxations were used to derive local minima, and stopped with a convergence threshold of 10^{-5} eV for self-consistency and 1 meV for energy changes in two consecutive self consistent field (SCF) steps.

In order to assess energy barriers and transition state (TS) structures, we carried out three consecutive steps of TS searches where nudged elastic band (NEB)[34] and climbing image NEB (CI-NEB)[35] were applied. We first performed NEB calculations with six images to estimate coordinates and energies along the reaction path. The initial (IS) and final state (FS) were fixed in the NEB@DFT search to accelerate convergence and reduce computational time. We then performed a second NEB in the restart mode in the Quantum Espresso[27] package with 12 images to acquire accurate reaction coordinates and energies. In the third step, we further refined the TS structure and its energy at a saddle point by performing a CI-NEB with the coordinates taken from the previous NEB simulations. We so obtained the reaction path between IS and FS as well as the energy barrier, calculated as the difference in energy between the TS and the IS.

The climbing image NEB (CI-NEB) calculations were performed employing a force convergence threshold of 0.05 eV Å^{-1} for all images (path_thr), in conjunction with an SCF energy convergence of 1 meV. It is useful to note that the climbing image, corresponding to the TS, was additionally converged using the default *fcp_thr* = 0.01 eV Å^{-1}, as implemented in the code. This approach ensures that the maximum force acting on the final climbing point, that is, the saddle point candidate, is minimized to within a stricter tolerance.

Although vibrational frequency analysis was not performed due to its computational cost, the TS structures were validated using the CI-NEB approach.[35] These include: 1) a well-defined energy maximum at the climbing image; 2) a smooth minimum energy path between reactant and product states, and 3) convergence of forces, with the climbing image relaxed to within 0.01 eV Å^{-1}, ensuring that it accurately represents the saddle point.

The NEB "nudging" scheme–which includes only the perpendicular component of the true force and the parallel component of the spring force–prevents artifacts such as corner-cutting and sliding-down, ensuring the integrity of the path.

In a selected case, we also performed Ab initio molecular dynamics (AIMD) simulations using Quantum Espresso within the Born–Oppenheimer approximation.[36]

2.1. Structural Motifs of TM_4 and TM_6 Clusters

At the basis of our study stands the definition of structural motifs. A structural motif is a basin of cluster configurations close to each other according to a certain distance metrics and within a given numerical threshold. In this study, we derived a set of structural motifs for tetramer and hexamer clusters, illustrated in **Figure 1**. The choice of structural motifs is also based on previous systematic work and analysis.[12] To make the search more systematic, we used templates of these structural motifs realized with the coordinates of Fe_4, Co_4, Au_4 elements for tetramers and of Pt_6, Cr_6, Ag_6, Nb_6, Os_6, Ti_6, and Ir_6 elements for hexamers, respectively, and obtained the initial coordinates of each motif for a new element via affine rescaling transformations.[37]

Note that for the tetramer we found it useful to define a "distorted pyramid" structural motif, that is, a 3D arrangement similar to a pyramid, but exhibiting significantly unequal nearest-neighbor distances. Analogously, in hexamers, a distorted Bi-pyramid structure is defined. We observe in this connection that, in general, some systems are expected to undergo Jahn–Teller distortions due to nonuniform occupancy of degenerate electronic levels.[38,39] To provide a simple but informative explanation of this effect, in the Supporting Information we examined the distortion from square to rhombus geometries using a Hückel model, showing that under general circumstances *s*-type systems must actually distort the symmetric square geometry to a rhomboidal one.

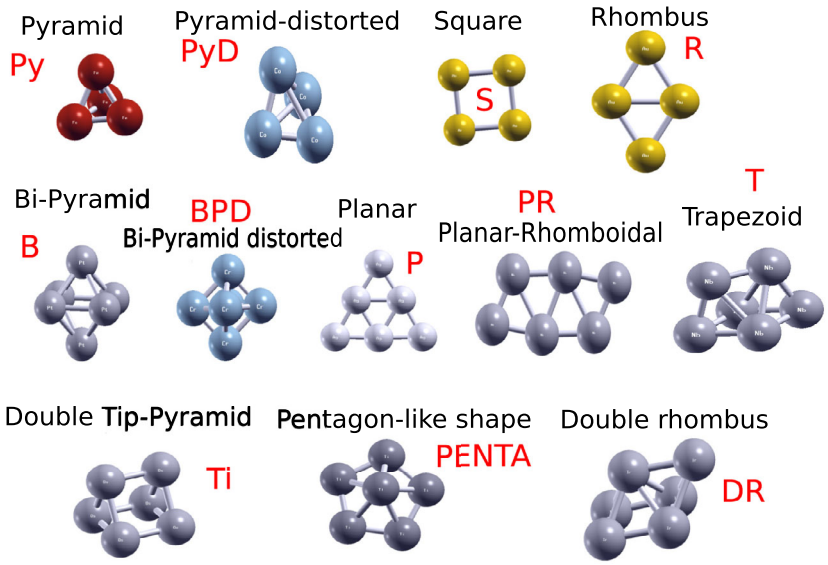

Figure 1. Initial geometries used after affine rescaling transformations for other TM. The top structures, from left to right, represent a pyramid [Py] (Fe_4), a distorted pyramid [PyD] (Co_4), a rhombus [R] (Au_4), and a square [S] (Au_4). The following two rows, from left to right, represent a Bi-Pyramid [B] (Pt_6), a distorted Bi-Pyramid [BPD] (Cr_6), a Planar [P](Ag_6), a Planar Rhomboidal [PR] (Nb_6), a Trapezoid [T] (Nb_6), a Double Tip Pyramid [Ti] (Os_6), a Pentagon-like shape [PENTA] (Ti_6), and a Double Rhombus [DR] (Ir_6).

3. Results and Discussion

Geometry relaxations were first conducted for tetramers and hexamers of all TM, producing an ensemble of local minima, the starting point of our analysis. For each element, each obtained local minimum was labeled according to one of the structural motifs illustrated in Figure 1 according to the following acronyms. $n = 4$: Pyramid (Py), distorted Pyramid (PyD), Rhombus (R) and Square (S); $n = 6$: Bi-pyramid (B), distorted Bi-pyramid (BPD), Double Tip Pyramid (TI), Planar (P), Double Rhombus (DR), Planar Rhomboidal (PR), Pentagon-like shape (PENTA) and Trapezoid (T). For comparison, the structural motifs of 55-atom clusters[11] are: icosahedral (ico), hcp/irregular icosahedral (irico), polytetrahedral (ptet), and fcc/close packed (cp), while those of bulk metals[40] are: face centered cubic (fcc), hexagonal closest packed (hcp), body centered cubic (bcc) and rhomboidal (rhomb). This nomenclature is used in **Figure 2** and throughout the article.

Note that, despite properly initializing the geometry, not all relaxations resulted in a locally stable configuration that retains the same motif as the starting configuration, as the given element may not possess the corresponding local minimum, so that the geometry optimization process ended up in a local minimum with a different morphology. Therefore, we had to devise appropriate descriptors to classify the obtained local minima into structural motifs irrespective of the initial input. To this purpose, we have employed geometry parameters, including dihedral angles, average distance, the ratio between the largest and average distance, and the number of angles within a certain range of values important within the characteristic of each motif. An unequivocal classification into the 12 structural motifs illustrated in Figure 1 has been so developed. Note that in Table S1, Supporting Information, we include the quantitative ranges in the values of the descriptors which we used to identify the various structural motifs in the decision tree in Figure S1, Supporting Information. Further details on the definition of descriptors and the construction of the classification/decision tree and confusion matrix can be found in the Supporting Information.

To better understand our descriptor-based classification and single out the most useful descriptors, we report confusion or error matrices (a nomenclature we borrow from Machine Learning literature) as Table S3–4, Supporting Information. We can observe that, in general, the most significant descriptors are the interatomic distances and the dihedral angles. In some cases, the number of dihedral angles and the largest/shortest distance ratio are also relevant, depending on the specific motif.

3.1. Morphology at the Subnanoscale

We start by exploring if a correlation exists between the structures of the lowest-energy configurations of subnanometer clusters and the lowest-energy structures of the corresponding bulk TM or 55-atom clusters. Note that this working hypothesis is stronger than the one explored in the work done by Rapps et al.[11] due to the very small size of the systems here investigated, in the extreme nanoscale régime.

Figure 2 compares the structural motifs of the global minima of tetramers (Figure 2a) and hexamers (Figure 2c) with the bulk thermodynamically favored phases as predicted by our DFT approach, as well as with the 55-atom cluster motifs (Figure 2b for tetramers, and 2d for hexamers, respectively) in the form of a restricted periodic table of the elements. Each element is assigned a rectangle in the table, divided by a cross-diagonal into two sections, in which the bottom-right one reports the structural motif of the global minimum of the subnanometer cluster, while the top-left one reports the

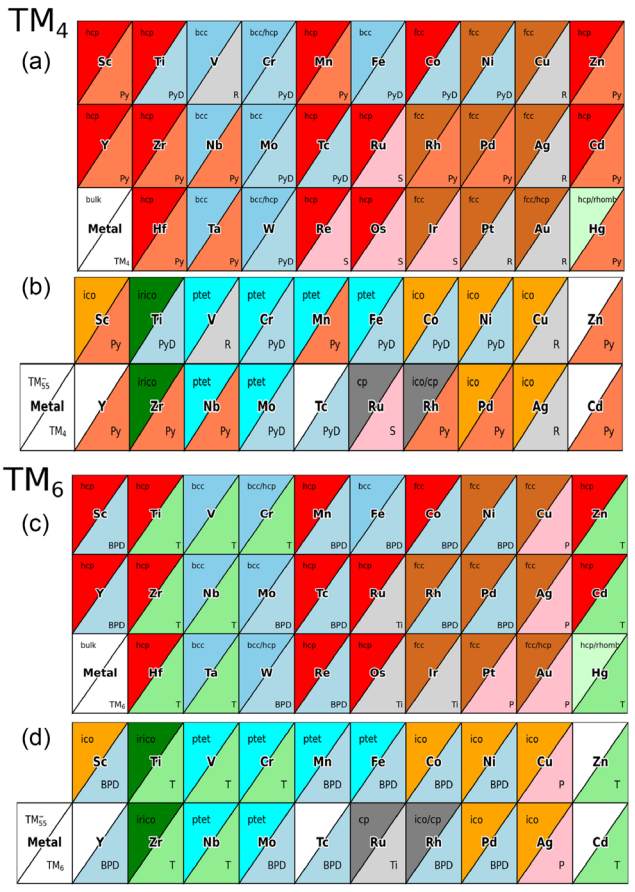

Figure 2. Comparison of our global minimum TM $_{n=4,6}$ with respect to our DFT bulk (panel "a" and "c") and anion TM of 55 atoms[11] (panel "b" and "d") respectively. Some chemical elements (Cr, W, Au, and Hg) have two bulk phases that are different by less than 5 meV. They are separated by a slash ("/"), and the deepest part is on the left.

corresponding bulk or 55-atom cluster motif.[11] For visual immediateness, each structural motif is also highlighted with a different color: $n = 4$: Py = coral, PyD = light-blue, R = light gray, and S = pink; $n = 6$: BPD = light-blue, TI = light gray, P = pink, and T = light-green; bulk: fcc = chocolate, hcp = red, and bcc = skyblue, and rhomb = light-green; 55-atom anions: ico = orange, irico = green, ptet = cyan, cp and ico/cp = gray.

Along each row, the experimental bulk structures[40] evolve regularly in the order: hcp → bcc → hcp → fcc → hcp, traversing the periodic table from left to right, except for the last row where the unit cell of bulk Hg is rhomboidal (rhomb). Note however, that, for the sake of internal consistency, we do not use experimental bulk phases but rather the bulk energies predicted via the same DFT/PBEsol computational approach employed for subnanometer clusters, that is, by local geometry relaxation of each structural motif for each element, corresponding to zero temperature predictions (0 K), **Figure 3** and **4** for a comparison. Note that our calculations predict higher binding energies than in experiment,[40] due to the limitations of our DFT approach and finite-temperature effects. In this regard, more precise DFT approaches could be employed for individual elements; however, the present study aims to provide a collective description.

Focusing on subnanometer clusters, an interesting trend emerges when the rows are scanned from left to right, similarly as in the bulk. For the tetramers, the sequence is Py → PyD → Py → PyD → R → Py for the first row; whereas Py → PyD → Py → R → Py for the second row. Exceptions are V (R) and Ru (S) in the first and second row, respectively. In the third row, the sequence is Py → PyD → S → R → Py. For the hexamers, the sequence is BPD → T → BPD → P → T, for TM belonging to the row Sc–Zn and Y–Cd, except Ru; while in Hf-Hg row, the sequence is T → BPD → TI → P→ T. Further trends are pictorially illustrated in **Figure 5**. For instance, the elements Fe, Mo, and W exhibit a common pattern, demonstrating an evolution from TM_n ($n = 4, 6, 55$) to bulk as a distorted pyramid to bi-pyramid to "ptet" and "bcc" phase. Noteworthy W_{55}^- and the TM marked with an asterisk (*) are not reported in the work by Rapps et al.[11] Therefore, tungsten-55 may manifest a "ptet" conformation in accordance with this trend.

Apart from exceptions due to spin phenomena (as we will see below, Section 3.4), we thus find correlations between the bulk and subnano trends. This observation supports our working hypothesis, which posited that the correlation between chemical elements and structural motifs observed for 55-atom anions[11] can be extended to the subnanometer scale, suggesting the existence of intrinsic properties that govern the structural landscape across length scales, from the subnano to the macro.

It is thus interesting to compare in more detail our results with those by Rapp's et al.[11] who researched the structures of 55-atom anionic clusters for some of the TM, showing that for TM_{55}^- the structural motifs generally correlate with bulk lattice types. In that case, bulk fcc elements form icosahedral clusters (ico), whereas for us (Ni,Pd and Rh) as well as (Cu and Ag) form a pyramid/bipyramid and rhombus/planar, for TM_4/TM_6, respectively, see Figure 2b,d. In contrast, some "bcc" elements (Mo and Fe) maintain their pyramidal-like structure upon increasing the size. The most stable configuration for V_4 is a rhombus, similarly to Cu_4, Ag_4, and Au_4. Interestingly, we observe a transition to a nonplanar, trapezoid motif for the global minimum of V_6, in contrast to the still planar lowest-energy configurations of Cu_6, Ag_6, and Au_6. The reason for this transition is that planar Cu_6, Ag_6 and Au_6 achieve electronic shell closure (spin $S = 0$), whereas the total magnetization of V_6 is $S = 2$, but transitions to $S = 0$ in the nonplanar structure. This prevalence of the rhombus with respect to the square is consistent with the Hückel model analysis discussed below and in the Supporting Information. In the sequence from $Sc_{4,6}$ to $Ti_{4,6}$ to $Co_{4,6}$, a transition in motif becomes evident that bears a notable similarity to that found in Ref. 11. In contrast, Zn, Zr, Hf, and Y exhibit a similar trend, with the exception of Y_6. However, technetium's behavior is analogous to titanium as TM_4, and to scandium as TM_6, while Ru shows a distinct tendency, transitioning from a planar (Ru_4: square) to a 3D (Ru_6: double-tip pyramid) structure, interestingly as also seen for Ru_{55}^-.

A close examination of bcc elements reveals a discernible trend that can be categorized. The transition of Fe, Mo, and W from a pyramid (TM_4) to a distorted pyramid (TM_6) is observed. Similarly, V_4, Cr_4, Nb_4, and Ta_4 transition from a pyramid

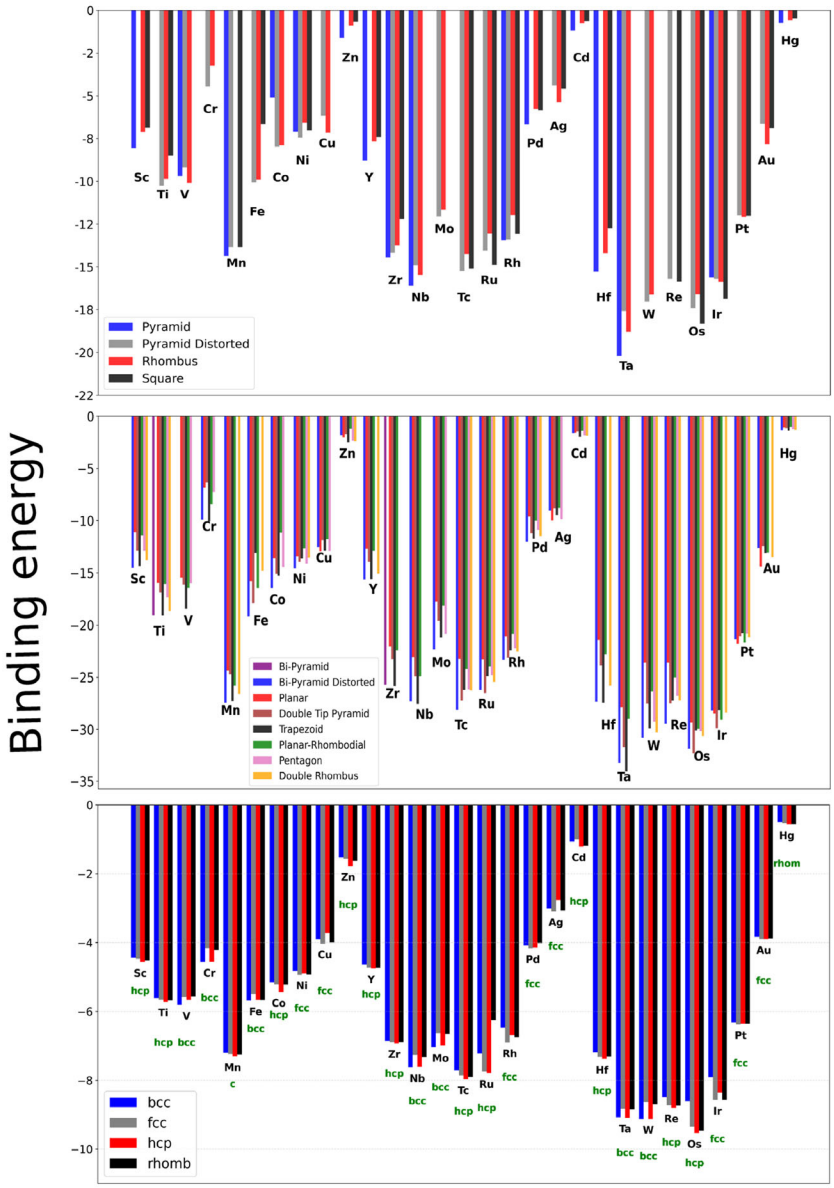

Figure 3. Binding energy as a function of the atomic number for TM_4 (top), TM_6 (middle), and bulk (bottom) according to the descriptor classification. The experimental bulk phase is highlighted in green.

(with the exception of V_4, which is a rhombus) to a trapezoid (TM_6). A distinction between these two groups may be at first based on their electronic properties and the arrangement of their electrons when the number of atoms is increased. To illustrate this point, consider that the total magnetization of the first group (Fe, Mo, and W) increases or remain constant, when the size of the cluster increases from four to six. In contrast, a decrease in magnetization is observed for the other group. However, magnetization alone is not sufficient to explain the observed trends, as evidenced by the cases of Mo and W from the first group, where the total magnetization is 0, and Nb and Ta from the second group, where Nb_6 has a magnetization of 2 and Ta_6 has a magnetization of 0. Further elucidation is necessary. An explanation based on electronic properties can then be found by examining the Mulliken electronegativity (ME): as demonstrated in the Table S14-15 and S16-17, Supporting Information, the ME of niobium and tantalum increases when cluster size increases, whereas that of molybdenum and tungsten decreases.

3.2. Crossover Among Structural Motifs

Our second target is to understand not simply the global minima but also the low-lying isomers, focusing on the energy gaps among them (this subsection) and the energy barriers in the transition from one to another (the next subsection). These quantities are critical in catalysis, where reaction mechanisms may imply such transformations, so that the catalytic performance depends

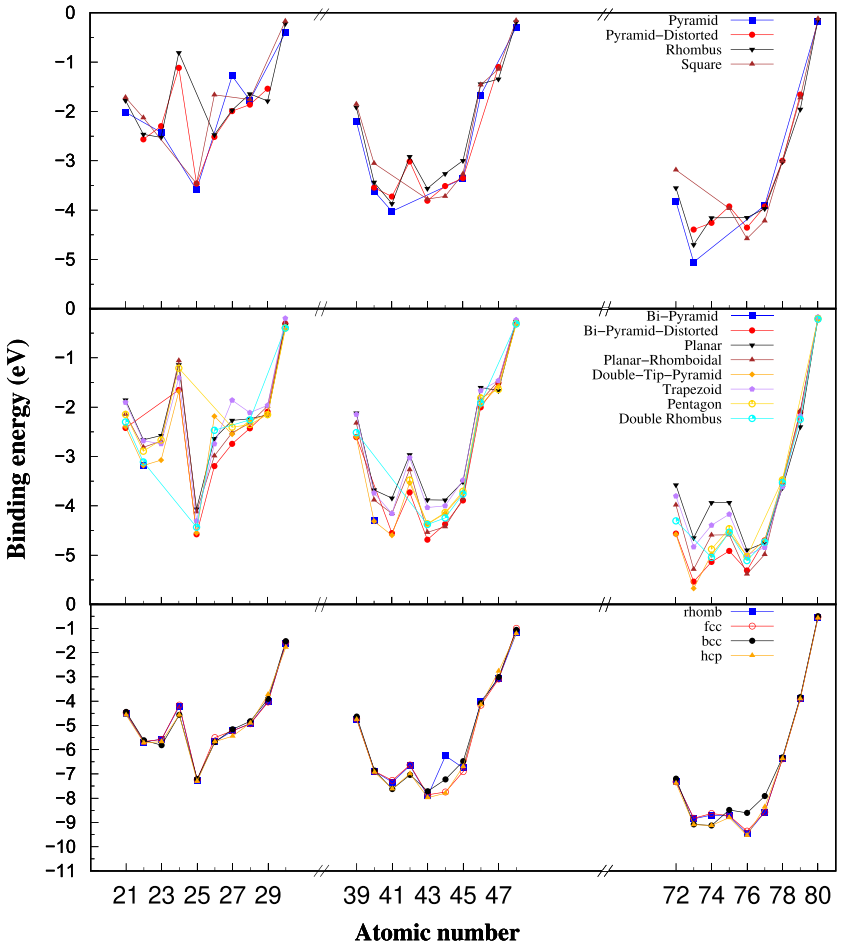

Figure 4. Binding energy crossover for TM $n = 4$ (top panel), 6 (middle panel), and bulk (bottom panel).

on the ordering and transitions of the low-lying configurations of ligand/cluster/support catalytic systems,[18–24] or, in other words, on their fluxional character.[24,25] Figure 3 reports the binding energies of all the local minima produced by our geometry relaxations as a function of atomic numbers: for tetramers (Figure 3a) and hexamers (Figure 3b), respectively, compared with the same quantities for bulk systems (Figure 3c). In instances where a specific motif was not observed and is therefore absent due to metastability, a blank space is inserted between the bars. For convenience of the reader, a different way of visualizing the crossover among structural motifs (crossover plots)[41,42] is presented in Figure 4 as well as the fluxional energies for the global minimum (Figure S3 and S4, Supporting Information).

We can once more recognize a discernible trend in the data reported in Figure 3. In the first row of TM of the periodic table (Sc—Zn), the binding energy increases from Sc to Ti and remains nearly constant with V. After vanadium, the curve of Figure 3 exhibits a decrease for Cr and an increase for Mn, then falls continuously until it reaches Zn. Note that $Sc_{4/6}$, $Mn_{4/6}$ exhibit both a subnanometer pyramidal shape (pyramid/bipyramid for TM_4 and TM_6 respectively) and a bulk "hcp" phase, see Figure S5, Supporting Information. In the second group (Y–Cd), the binding energy exhibits an increase from Y to Nb, a decrease for Mo, an increment for Tc, and a subsequent gradual decay until Cd, both in subnano and bulk configurations. Within this block, Y_4 and Tc_4 maintain their pyramidal shape, while Nb_4 transitions from a pyramidal to a trapezoidal structure. The last group (Hf–Hg) behaves mainly like the first group, increasing in binding energy from Hf to Ta and reducing to Re, showing a peak in Os and further decreasing until reaching Hg. Note that Hf_n and Ta_n go from a Pyramid ($n = 4$) to a Trapezoid ($n = 6$), while in the bulk Hf corresponds to a "hcp" and Ta and W to a "bcc" motif. In contrast, osmium undergoes a transition from a planar structure to a 3D structure (from Os_4: Square, to Os_6: double-tip pyramid).

This transformation is concurrent with the hexamer acquiring a nonzero total magnetization, as opposed to the absence of magnetization in the four-atom system (see Figure S21, Supporting Information and its discussion). As can be evinced from Table S6, Supporting Information, Os_6 possesses two local minima that belong to the same deepest motif and can be explained in terms of magnetization effects, see Section 3.4. A similar phenomenon is observed for $Ru_{4,6}$. As for V_6, the formation of an additional structure that belongs to a distinct isomer type necessitates a more intricate electron arrangement.

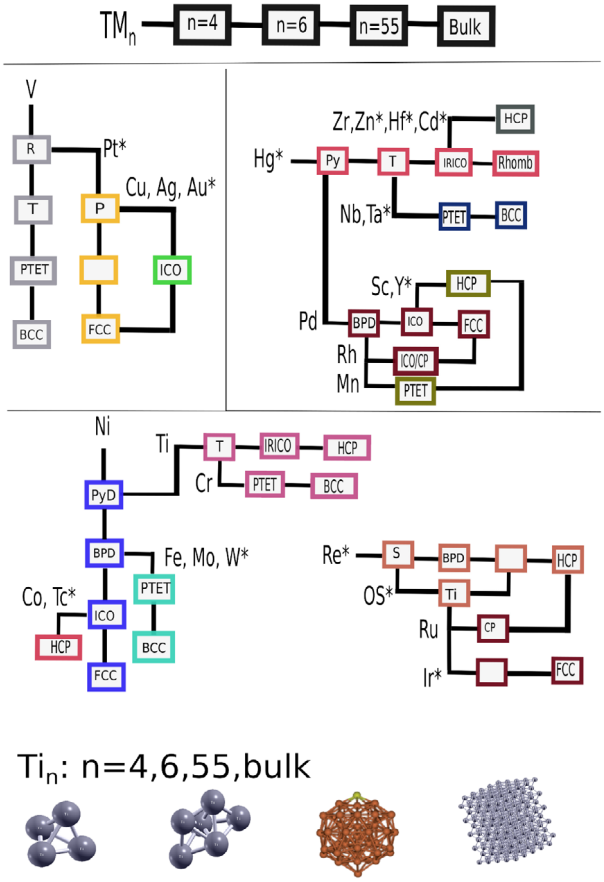

Figure 5. TM trends from TM_n $n = 4, 6$ and bulk (present research), and TM_{55}^- from Ref. [11]. The TM marked with an asterisk (*) indicate that TM_{55}^- has not been previously reported. The illustration of evolution (Ti) is located at the base of the crossover trends.

3.3. Square and Rhombus Motifs

The deformation of the square motif into a rhomboidal one is an instance of the Jahn–Teller effect,[38] which posits that any nonlinear molecule possessing a spatially degenerate electronic ground state will undergo a geometric distortion to eliminate the degeneracy and reduce its total energy. As anticipated above, this deformation can be understood in terms of a simple Hückel's approach.[43–45] In the Hückel's approach, the total energy is a sum of one-electron energies from a simplified single-particle Hückel Hamiltonian. We define the deformation energy as the difference between the total energy of the rhombus and square shapes, where a negative value indicates that deformation from a rhombus to a square is energetically favored. In the Supporting Information we show that, by postulating that the Hückel Hamiltonian matrix elements depend exponentially on the interatomic distance (setting overlap integrals equal to zero), and for simple metals exhibiting only *s*-type interactions, it is energetically favorable for the square motif to deform into a rhombus. Our assumptions are that resonance integrals are equal to $\beta = H_{ij}$ depending exponentially on interatomic distance.

Löwdin charges offer further information on the rhombus versus square competition, and have been reported in Table S26–27, Supporting Information, complementing Table S28–29, Supporting Information, where the Löwdin charges and the projected density of states (DOS) are reported, respectively. Table S26, Supporting Information, reports Löwdin charges for elements that have a deeper-energy square shape compared to a rhombus one. They present an increase in populations of the "p" and "d" orbitals with decreasing populations in the "s" orbitals for the rhombus shape, leading to occupancy of higher levels and less binding energy. An outlier case is Rh_4.

According to the Löwdin analysis, the charges in the rhombus shape are predominantly located in the orbitals "pz" and "dz2", which can be attributed to a sort of repulsion, a consequence of the Pauli exclusion principle. In Table S27, Supporting Information, that shows Löwdin charges for elements that have a deeper-energy rhombus shape, a distinct scenario emerges. In this case, a subset of atoms exhibit a decrease in population of the "d" orbitals, accompanied by an increase in population of the "s" orbitals. This phenomenon is opposite to the behavior observed in Table S26, Supporting Information. Finally, a nonzero magnetization can also play a role, as it can result in one of the following motifs either square or rhombus: Sc, Ti, Fe, Ni, Tc, and Ir. In Figure S23, Supporting Information, the DOS is illustrated as a function of energy and its projection onto each type of orbital involved (*s*, *p* and *d*). It can be seen that, for Ni_4 and Rh_4, the *d* orbitals form stronger bonds than in Y_4, thereby favoring the square over the rhombus shape. This phenomenon occurs in about 3/4 of our clusters, whereas elements such as Ru_4, Re_4, Os_4, and Ir_4 have as ground-state isomer in a square form.

3.4. Stability of the Global Minima, Electronic Properties, and Magic Clusters

In Figure S7, Supporting Information, the stability of the isomers was assessed by plotting the energy crossover among motifs. We now focus on a subset of these energies to gain insight on the stability of the global minima. In **Figure 6** we graph the energy gap, that is, the energy difference between the two lowest-energy isomers (belonging to either the same or different motifs) as a function of atomic number for tetramers (Figure 3, 6, top) and hexamers (Figure 3, 6, middle), compared with the corresponding bulk quantities (Figure 3, 6, bottom). In some cases, the two lowest-energy isomers do not belong to the same structural motif, as illustrated by the discrepancy between red and black dots for Ti_4, V_4, Cr_4, Mo_4, Pd_4, W_4, Au_4 and V_6, Fe_6, Co_6, Mn_6, Nb_6, Mo_6, Ru_6 and Ta_6. When such a discrepancy is large, this means that the cluster can rearrange easily within the energy basin defined by one structural family, but has to overcome a barrier to change its shape qualitatively.

The trend in the plots of Figure 6 can be explained in terms of the electronic properties of the clusters, such as their work function (the energy to remove an electron and bring it to infinity[46]), that we calculate as the difference between the electrostatic Coulomb potential in vacuum and the Fermi energy. We also calculated additional electronic property, namely ME (that quantifies the ability of an cluster to attract and retain electrons) and hardness, associated with the highest occupied molecular orbital

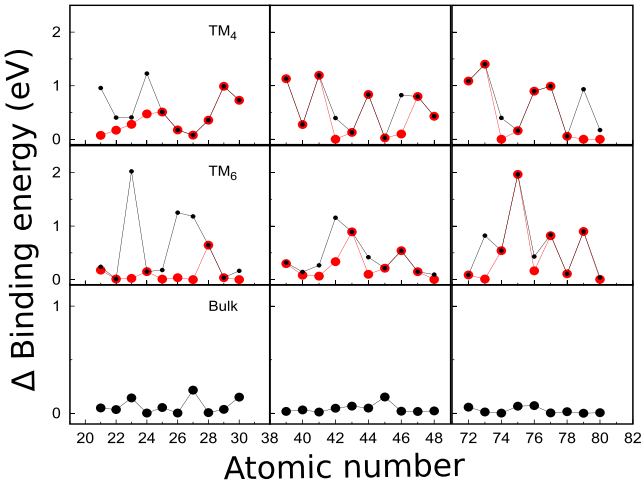

Figure 6. Binding energy difference for the two lowest-energy isomers of TM_n, in red circles: (TM) $n = 4$ (top panel) and $n = 6$ (middle panel). Black dots correspond to the difference between the two lowest-energy isomers belonging to different structural motifs, including bulk (bottom panel).

and lowest unoccupied molecular orbital (HOMO–LUMO) gap (see Table S8-11, Supporting Information) and which describes the resistance of an atom to a change of its electronic state. A small HOMO–LUMO gap usually indicates a higher degree of reactivity, while a substantial gap is indicative of enhanced stability (systems evolves toward a state of maximum hardness).[47–49] Clearly, for magnetic clusters these quantities will split into spin up and spin down, as illustrated for Fe_6 in Figure S8, Supporting Information, exhibiting a total magnetization (difference between electrons with spin-up and spin-down) equal to 20. Despite the conceptual similarity between HOMO–LUMO and hardness, it is possible to discern differences between them. The HOMO–LUMO gap provides insight into frontier orbital energetics, while chemical hardness (η) better captures the system's stability and reactivity under adsorption and catalytic conditions, as it directly measures resistance to charge transfer and electronic cloud deformation, in keeping with known theorems.[50]

The trend in energy gaps as a function of the atomic number was divided into three segments by distinguishing between spin up/down, as illustrated in Figure S10, S15 and S20, Supporting Information. In the TM first row, trends in energy gaps resemble the pattern observed in the electronic properties. For instance, the hardness curve with spin-down in TM_4 displays a comparable profile with respect to the binding energy. However, a comparison of the work function with the other electronic trend reveals its closer alignment with the ME with spin-down. Regarding TM_6, the ME with spin-up clearly correlates with the binding energy, with the exception of Sc_6-Fe_6, which instead correlate with the hardness with spin-down. The work function is then well reproduced by the ME spin-down. In the next block, including the second-row TM, the binding energy gap and work function mainly correlate well with the ME both spin up and down for cluster size of 6 atoms. In contrast, for Y_4-Nb_4 and Ru_4-Pd_4 the ME is the best candidate to explain gap trends, while for Mo_4-Ru_4 and Pd_4-Cd_4 these are better explained by the hardness for spin up and down respectively. The third-row TM block reproduces the trend of both TM_4 and TM_6 for the pattern seen in Figure 6, and for the work function for the TM_4 systems. The ME with spin-down agrees much better with the work function for six-atom TM.

In addition to the "maximum hardness principle," (correlated with the HOMO–LUMO gap) the "minimum softness principle" or its alternative, the "minimum polarizability principle," can be considered. This principle states that the polarizability of a stable molecule at its equilibrium structure should be less than the sum of the polarizabilities of its constituent atoms. However, spin magnetization complicates the picture, as in spin-polarized systems electronic interactions occur via spin majority and minority channels. We can for example, define and use in our analysis spin-polarized HOMO–LUMO gaps, that is, separate HOMO–LUMO gaps in the majority and minority spin channels. Finally, it is clear that the nearly degenerate orbitals the system will produce high-spin, resulting in low polarizability and significant hardness.[50] In our dataset, this phenomenon is exemplified by Ru_6 and Os_6, see Figure S18 and 19, Supporting Information.

The spin polarization plots for the Os_6 cluster offer significant insights into its magnetic and electronic structure. The plot on the left of Figure S21 in Supporting Information, corresponding to a low isosurface value (0.0007 [e^-/Bohr^3]), demonstrates a uniform and extensive distribution of the spin density, suggesting that unpaired electrons are delocalized across the entire cluster. This observation suggests the presence of collective magnetic behavior and delocalized bonding between the osmium atoms. In contrast, the right plot, with a larger isosurface value (0.007 [e^-/Bohr ^{3}]), highlights more localized regions with strong spin polarization, indicating specific atoms or bonds where unpaired electrons are concentrated. This fragmented appearance suggests the presence of directional or anisotropic spin polarization, associated with specific d-orbitals. The coexistence of both delocalized and localized spin density suggests a complex electronic structure, which is characteristic of open-shell metallic systems. This information can be useful to understand the reactivity and potential applications of Os_6 clusters in catalysis or molecular magnetism.

As can be seen by inspecting Figure S16 and S17, Supporting Information, 2D structures, such as a rhombus or square for TM_4 and planar structures (Planar and Planar Rhomboidal) for TM_6, seem to correlate their being the global minima with a strong increase in the hardness ($Cu_{4,6}$, $Ag_{4,6}$, Ru_4, Pt_4 and $Au_{4,6}$). Cases with nonzero spin magnetization, such as V_4 and Ir_4, are more complicated. In these cases, the HOMO–LUMO gap is decreased, and the global minima tend to correspond to the motifs for which the ME is largest. Other cases are those in which maximum hardness is reached together with a magnetic state, such as Re_4 and Ir_6. An exception to this rule is Os_4, in which the presence of different motifs is correlated with different kinds of spin orientations, thereby with HOMO–LUMO gaps varying in a wide range. This analysis is meant to be in perspective, since HOMO–LUMO gap and hardness play an important role in determining the interaction of these transition metal clusters with adsorbates, see for example, the work done by Kateris et al.[51]

3.5. Magic Cluster

Of particular interest are the systems for which the energy gap is large, as these are highly stable "magic" clusters that could maintain their shape for extended periods of time. Indeed, by defining the activation energy barrier of a cluster transformation between two isomers, E_a, as the larger barrier for the given transformation, while the barrier for the backward transformation will be given by this value minus the energy difference between the two isomers (ΔE), and by using the Arrhenius Equation,[51] we can estimate the rate constant of the transformation as

$$K_A = Ae^{-E_a/k_B T} \quad (1)$$

where k_B is the Boltzmann constant, and T is the absolute temperature. The Arrhenius prefactor has not been calculated explicitly; rather, an estimated value of $10^{12} - 10^{14}\,\mathrm{sec}^{-1}$ has been utilized.[53,54] Then, the half-life of the transformation reaction is calculated as

$$t_{1/2} = \frac{\ln(2)}{K_A} \quad (2)$$

and can require a time span exceeding months at room temperature if $E_a > 1.1$ eV.

Let us focus as an example on one of the elements and sizes for which the energy gap is highest, that is, Re_6, which exhibits an exceptionally stable BPD global minimum, with an energy gap of nearly 2 eV to the first isomer, of TI shape. We have used the NEB and Climbing Image NEB (CI-NEB) methods[34,35] to calculate the barrier for the TI → BPD transformation. The resulting NEB energy profile for Re_6 with nonzero spin magnetization (spin = 2) is shown in **Figure 7**. Note that in a NEB it is necessary to fix the total magnetization during the path, whereas in a MD run the magnetization can in principle fluctuate. To further confirm the stability of the Re_6 BPD global minimum as well as to sample geometries that may have been overlooked by our local relaxations, we have then conducted AIMD simulations for Re_6 using quantum Espresso within a Born–Oppenheimer approach.[36] A Berendsen thermostat was used to regulate the temperature at 600 K during the AIMD simulation, and the root mean square deviation of the atomic positions with respect to the final geometry of the simulation is plotted in Figure S27, Supporting Information. As illustrated in the Figure S27, Supporting Information, the TI initial state of Re_6 at a temperature of 600 K evolves toward a TI state with different spin magnetization (from 0 to 2, see the Supporting Information), which is a relatively stable local minimum, and then remains there for the following 35 ps - based on the NEB energy barrier and the Arrhenius approach, the cluster should remain in the local minimum isomer for at least ≈1200 ps until it transitions to the global minimum (BPD). Analogous NEB simulations have been conducted for other interesting cases, that we do not report here for reasons of space.

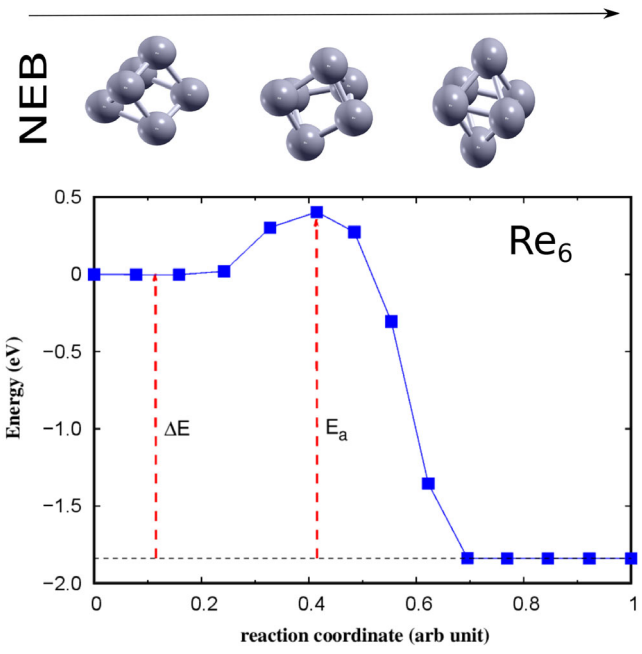

Figure 7. CI-NEB calculations for Re_6 with total magnetization equal to 2. Energy is given in eV as a function of a reaction coordinate (arb unit).

4. Conclusions

Understanding and manipulating matter at the subnanometer scale remains a formidable task, although needed to fully exploit the potentialities of these systems, such as TM subnanometer catalysts, that are of extreme interest in the energy and environmental fields.[2–6] Moreover, these systems have been extensively studied due to their remarkable structural, photophysical, and redox properties.[55–57] Some of their properties, such as stability, high photoluminescence, large Stokes shifts, and therapeutic potential, make them appealing in biological applications. Elements such as iron(III), cobalt, and vanadium have a potential for designing luminescent metal probes, particularly for bioimaging and biosensing. The coordination of metal cations to organic ligands with low-lying unoccupied π^* orbitals opens then a path for achieving long-lived phosphorescence in metal-to-ligand charge-transfer excited states.

In the present work, we address the problem of understanding the structural and electronic properties of selected subnanometer clusters of TM via a two-step strategy: 1) we conduct systematic first-principles calculations to predict the low-energy atomistic configurations (local minima) of TM tetramer and hexamer clusters with their energetics (including selected transformation barriers) as well as features of their electronic structure (electronegativity and hardness) and 2) we analyze the resulting data in the search for both patterns and outliers in structure, energy, and properties, also comparing with bulk morphologies and existing information on larger (55-atom) clusters, and trying to rationalize both trends and exceptions to the observed trends.

Concerning task (i), the 4- and 6-atom cluster database we derive (also shared via a dedicated Web site)[26] integrates and significantly extends previous theoretical studies[12] and should be useful as a reference for future studies, providing a basis for further analyzes or initial configurations and energetics to investigate cases in which these confined objects are immersed into an interacting environment (solvents, ligands, supports).

From the analysis of the so-derived database, we also draw promising conclusions.

First, despite dealing with the extreme and usually considered nonscalable régime of cluster science, we do find trends and correlations that link structural motifs at the subnanoscale with those typical of larger, even macroscopic length scales, with similar observations holding also for more subtle energy quantities, such as the energy differences between global minimum and lowest-lying isomer, crossover among structural motifs, and, to a lesser extent quantities related to the HOMO–LUMO energy gap (electronegativity and hardness). These findings reveal that there are intrinsic structural motifs evolving with size from the subnanoscale to the bulk, as suggested in a previous study,[11] therefore linking nanometer and mesoscopic forms of matter.

Second, we also search for and encounter outliers, that is, exceptions to these trends in terms of energy and/or structure. The "magic clusters", such as Re_6, viz. outliers with an unusually high difference between global minimum and lowest-lying isomer, are one class of systems we are interested in, since they are predicted to maintain their shape for long periods of time (even macroscopic) at moderate temperatures. Also, they are often associated with enhanced stability, so as to represent a maximum (spike) in the formation energy diagram as a function of size thus acting as accumulation and/or nucleation centers.[20] In the opposite perspective, for specific catalytic functionalities one can be interested in robust but "fluxional" systems,[24,25] so that we also provide information useful to classify these cases, moreover distinguishing rapid transformations within a constant structural motif (related to the phenomenon of conical intersection)[22] from fluxionality across different structural motifs. Finally, we encounter outliers to structural trends along the periodic table, and we try to rationalize them in terms of electronic structure (*d*-bonding) considerations, where these systems are interesting because they present unique, nonscalable features that may be useful in some applications. For example, $TM_n = V$, Ru, Re, and Os transit from a 2D (TM_4) to 3D (TM_6). This transition is attributed to the emergence of a nonzero total magnetization, the existence of multiple conformations belonging to the deepest motif, and the subsequent rearrangement of their electrons according to their magnetization.

In summary, we hope that the present study can provide a framework and trigger further efforts to understand and eventually control and fine tune, the functionality of subnanometer cluster systems.

Supporting Information

Supporting Information is available from the Wiley Online Library or from the author.

Acknowledgements

This project has originated and has been developed within the COST Action CA21101 "Confined molecular systems: from a new generation of materials to the stars" (COSY) supported by COST (European Cooperation in Science and Technology). The authors are grateful to the Cineca Supercomputing Center (Italy) for providing computational resources. The authors acknowledge financial support under the National Recovery and Resilience Plan (PNRR), Mission 4, Component 2, Investment 1.1, by the Italian Ministry of University and Research (MUR), funded by the European Union - NextGenerationEU - Project COCAP. P.Z. was supported by the National Science Center (NSCN), project no. 2019/34/E/ST4/00407. We are very grateful to Lyudmila Moskaleva (University of the Free State, South Africa) for her insights on the design of this work.

Conflict of Interest

The authors declare no conflict of interest.

Author Contributions

Alessandro Fortunelli and **Piotr Zuchowski** conceived the project. **Alessandro Fortunelli** and **Ernesto Garcia-Alfonso** designed and implemented the computational study. **Ernesto Garcia-Alfonso** performed the calculations. **Thantip Roongcharoen** advised on computational methods and analysis of the results. **Ernesto Garcia-Alfonso**, **Alessandro Fortunelli**, and **Thantip Roongcharoen** analyzed the results. **Ernesto Garcia-Alfonso** wrote the first draft of the manuscript, then finalized with **Alessandro Fortunelli**, and all authors contributed to the final manuscript.

Data Availability Statement

The data that support the findings of this study are openly available in Github at https://github.com/piotrzuchowski/COSY_Inter_Nano/tree/main/clusters, reference number 5083804.

Keywords

binding energy, energy barriers, isomerization, subnanometer clusters, transitions metals

Received: May 27, 2025
Revised: July 7, 2025
Published online:

[1] Y. Lu, W. Chen, *Chem. Soc. Rev.* **2012**, *41*, 3594.
[2] A. Halder, L. A. Curtiss, A. Fortunelli, S. Vajda, *J. Chem. Phys.* **2018**, *21*, 148.
[3] E. Fernández, M. Boronat, *J. Phys. Condens. Matter* **2019**, *31*, 013002.
[4] Z. Luo, A. W. C. Jr, S. N. Khanna, *Chem. Rev.* **2016**, *116*, 14456.
[5] E. Yoo, T. Okata, T. Akita, M. Kohyama, J. Nakamura, I. Honma, *ACS* **2009**, *9*, 6.
[6] B. Peng, Z. Liu, L. Sementa, Q. Jia, Q. Sun, C. U. Segre, E. Liu, M. Xu, Y.-H. Tsai, X. Yan, Z. Zhao, J. Huang, X. Pan, X. Duan, A. Fortunelli, Y. Huang, *Nat. Catal.* **2024**, *7*, 818.
[7] C. Dessal, T. Len, F. Morfin, J. L. Rousset, M. Aouine, P. Afanasiev, L. Piccolo, *ACS Catal.* **2019**, *9*, 5752.
[8] F. Morfin, C. Dessal, A. Sangnier, C. Chizallet, L. Piccolo, *ACS Catal.* **2024**, *14*, 9628.
[9] Z. Y. Li, N. P. Young, M. D. Vece1, S. Palomba, R. E. Palmer, A. L. Bleloch, B. C. Curley, R. L. Johnston, J. Jiang, J. Yuan, *Nat. Lett.* **2008**, *451*, 3.
[10] P. Gruene, D. M. Rayner, B. Redlich, A. F. G. van der Meer, J. T. Lyon, G. Meijer, A. Fielicke, *Science* **2008**, *321*, 5889.
[11] T. Rapps, R. Ahlrichs, E. Waldt, M. M. Kappes, D. Schooss, *Angew. Commun.* **2013**, *52*, 6102.
[12] A. S. Chaves, M. J. Piotrowski, J. L. F. D. Silva, *Phys. Chem. Chem. Phys.* **2017**, *19*, 15484.

[13] Z. W. Seh, J. Kibsgaard, C. F. Dickens, I. Chorkendorff, J. K. Nørskov, T. F. Jaramillo, *Science* **2017**, *355*, 6321.
[14] J. Jašík, S. Valtera, M. Vaidulych, M. Bunian, Y. Lei, A. Halder, H. Tarábková, M. Jindra, L. Kavan, O. Frank, S. Bartling, Š. Vajda, *Faraday Discuss.* **2023**, *242*, 70.
[15] S. Vajdaa, G. P. Wiederrechta, A. Bouheliera, G. Y. Tikhonova, N. Tomczyka, B. Leec, S. Seifertc, R. E. Winansc, *Collect. Czech. Chem.* **2007**, *1*, 121.
[16] J. Hagen, L. D. Socaciu-Siebert, J. L. Roux, D. Popolan, S. Vajda, T. M. Bernhardt, L. Wöste, *Sci. Direct* **2007**, *261*, 152.
[17] Y. Lei, F. Mehmood, S. Lee, J. Greeley, B. Lee, S. Seifert, R. E. Winans, J. W. Elam, R. J. Meyer, P. C. Redfern, D. Teschner, R. Schlögl, M. J. Pellin, L. A. Curtiss, S. Vajda, *Science* **2010**, *328*, 224.
[18] F. R. Negreiros, L. Sementa, G. Barcaro, S. Vajda, E. Aprá, A. Fortunelli, *ACS Catal.* **2012**, *2*, 1860.
[19] A. Corma, P. Concepción, M. Boronat, M. J. Sabater, J. Navas, M. J. Yacaman, E. Larios, A. Posadas, M. A. López-Quintela, D. Buceta, E. Mendoza, G. Guilera, A. Mayoral, *Nat. Chem.* **2013**, *5*, 775.
[20] I. R. Arias, D. Buceta, G. Barone, M. C. Giménez-López, H. Lozano, M. Lazzari, M. A. López-Quintela, *J. Colloid Interface Sci.* **2022**, *628*, 437.
[21] L. L. Carroll, L. V. Moskaleva, M. P. de Lara-Castells, *Phys. Chem. Chem. Phys.* **2023**, *25*, 15729.
[22] K. M. Krupka, M. P. de Lara-Castells, *Phys. Chem. Chem. Phys.* **2024**, *26*, 28349.
[23] R. M. Martin, *Basic Theory and Practical Methods*, Press NYCU, Cambridge **2004**.
[24] F. R. Negreiros, G. Barcaro, L. Sementa, A. Fortunelli, *C. R. Chim.* **2014**, *7–8*, 625.
[25] Z. Zhang, B. Zandkarimi, A. N. Alexandrova, *Acc. Chem. Res.* **2020**, *53*, 447.
[26] COSY-NANO-DATA **2025**, GitHub, https://github.com/piotrzuchowski/COSY_Inter_Nano/tree/main/clusters (accessed: July 2025).
[27] P. Giannozzi, S. Baroni, N. Bonini, M. Calandra, R. Car, C. Cavazzoni, D. Ceresoli, G. L. Chiarotti, M. Cococcioni, I. Dabo, A. Dal Corso, S. de Gironcoli, S. Fabris, G. Fratesi, R. Gebauer, U. Gerstmann, C. Gougoussis, A. Kokalj, M. Lazzeri, L. MartinSamos, N. Marzari, F. Mauri, R. Mazzarello, S. Paolini, A. Pasquarello, L. Paulatto, C. Sbraccia, S. Scandolo, G. Sclauzero, A. P. Seitsonen, et al., *J. Phys. Condens. Matter* **2009**, *21*, 395502; Quantum ESPRESSO (Version 7.2) [Computer software]. https://www.quantum-espresso.org/.
[28] J. P. Perdew, K. Burke, M. Ernzerhof, *Phys. Rev. Lett.* **1996**, *77*, 3865.
[29] A. V. Terentjev, L. A. Constantin, J. M. Pitark, *Phys. Rev. B* **2018**, *98*, 214108.
[30] L. A. Constantin, J. P. Perdew, J. M. Pitarke, *Phys. Rev. B* **2009**, *79*, 075126.
[31] K. Laasonen, A. Pasquarello, R. Car, C. Lee, D. Vanderbilt, *Phys. Rev. B* **1993**, *47*, 16.
[32] D. Vanderbilt, *Phys. Rev. B* **1990**, *41*, 11.
[33] S. Grimme, J. Antony, S. Ehrlich, H. Krieg, *J. Chem. Phys* **2010**, *132*, 15104.
[34] G. Henkelman, H. Jónsson, *J. Chem. Phys.* **2000**, *113*, 9978.
[35] G. Henkelman, B. P. Uberuaga, H. Jónsson, *J. Chem. Phys.* **2000**, *113*, 9901.
[36] D. Marx, J. Hutter, *AB Initio Molecular Dynamics: Basic Theory And Advanced Methosd*, Cambridge University Press, Cambridge, UK **2009**.
[37] T. Roongcharoen, G. Conter, L. Sementa, G. Melani, A. Fortunelli, *J. Chem. Theory Comput.* **2024**, *9580–9591*, 20.
[38] H. A. Jahn, E. Teller, *Proc. R. Soc. London, Ser. A* **1937**, *161*, 220.
[39] S. V. Streltsov, D. I. Khomskii, *Phys. Rev. X* **2020**, *10*, 031043.
[40] C. Kittel, *Introduction To Solid State Physics*, John Wiley & Sons, Inc, Hoboken, NJ, USA **2005**.
[41] L. Sementa, G. Barcaro, F. R. Negreirosa, A. Fortunelli, *Phys. Chem. Chem. Phys.* **2014**, *16*, 26570.
[42] F. Baletto, R. Ferrando, A. Fortunelli, F. Montalenti, C. Mottet, *J. Chem. Phys.* **2002**, *116*, 3856.
[43] E. Hückel, *Z. Phys.* **1931**, *70*, 204.
[44] P. Atkins, J. de Paula, *Atkins' Physical Chemistry*, Oxford University Press, Oxford, UK **2006**.
[45] J. P. Lowe, K. A. Peterson, *Quantum Chemistry*, Elsevier, Burlington, MA, USA **2005**.
[46] J. Bardeen, *Phys. Rev.* **1936**, *49*, 9.
[47] V. H. Rezvan, *Results Chem.* **2024**, *7*, 101437.
[48] J. L. Gazquez, *Hardness and Softness in Density Functional Theory*, Springer-Verlag, Berlin **1993**, pp. 27–44.
[49] R. G. Pearson, *Acc. Chem. Res.* **1993**, *26*, 250.
[50] W. Grochala, *Phys. Chem. Chem. Phys.* **2017**, *19*, 30964.
[51] N. Kateris, R. Xu, H. Wang, *Combust. Flame* **2023**, *257*, 112513.
[52] R. Eisberg, R. Resnick, *Quantum Physics of Atoms, Molecules, Solids, Nuclei and Particles*, John Wiley & Sons, USA **1974**.
[53] H. Heinemann, *Reaction Kinetics and Reactor Desing*, Marcel Dekker, New York-Basel **2000**.
[54] K. J. Mintz, R. J. Cvetanovi, *Can. J. Chem.* **1973**, *51*, 3386.
[55] Y. Ning, G. Q. Jin, M. X. Wang, S. Gao, J. L. Zhang, *Curr. Opin. Chem. Biol.* **2022**, *66*, 102097.
[56] K. S. Kjær, N. Kaul, O. Prakash, P. Chábera, N. W. Rosemann, A. Honarfar, O. Gordivska, L. A. Fredin, K.-E. Bergquist, L. Häggström, T. Ericsson, L. Lindh, A. Yartsev, S. Styring, P. Huang, J. Uhlig, J. Bendix, D. Strand, V. Sundström, P. Persson, R. Lomoth, K. Wärnmark, *Science* **2019**, *363*, 249.
[57] M. Dorn, J. Kalmbach, P. Boden, A. Päpcke, S. Gómez, C. Förster, F. Kuczelinis, L. M. Carrella, L. A. Büldt, N. H. Bings, E. Rentschler, S. Lochbrunner, L. González, M. Gerhards, M. Seitz, K. Heinze, *J. Am. Chem. Soc.* **2020**, *142*, 7947.